

# Comparison of private flux region instability in conventional and super-X divertor configurations

D.A. Baver and J.R. Myra

*Lodestar Research Corporation, Boulder, Colorado 80301, USA*

F. Militello and D. Moulton

*CCFE, Culham Science Centre, Abingdon, Oxon OX14 3DB, United Kingdom*

July 2021, rev. Oct 2021

accepted for publication in the  
*Physics of Plasmas*

---

SC/0019270-2

LRC-21-189

---

**LODESTAR RESEARCH CORPORATION**

*5055 Chaparral Court, Suite 102*

*Boulder, Colorado 80301*

This is the author's peer reviewed, accepted manuscript. However, the online version of record will be different from this version once it has been copyedited and typeset.

PLEASE CITE THIS ARTICLE AS DOI: 10.1063/1.50063766

## Comparison of private flux region instability in conventional and super-X divertor configurations

D. A. Baver<sup>a)</sup>, J. R. Myra

Lodestar Research Corporation, Boulder, CO, 80301, USA

F. Militello, D. Moulton

CCFE, Culham Science Centre, Abingdon, OX14 3DB, UK

### Abstract:

Understanding turbulence in the divertor leg of tokamaks is essential to predicting the heat deposition profile on the divertor plate. This in turn is important for evaluating advanced divertor configurations, such as the super-X divertor. Within the divertor region, the private flux region is of interest because it is relatively unaffected by turbulence extending from the outboard midplane, so instabilities in this region could have a particularly pronounced effect on transport. These instabilities are modeled using the Arbitrary Topology Equation Reader (ArbiTER) eigenvalue code. Eigenmodes are examined further by comparing physics models to determine the fundamental mechanisms behind their formation, and quantifying the effect of individual terms. This analysis is conducted on both conventional and super-X divertors to compare these effects. The resulting analysis reveals the presence of a geodesic curvature driven instability that is significantly more pronounced in the super-X configuration.

Keywords: divertor, super-X, private flux region, tokamak, turbulence, ballooning

a) Author to whom correspondence should be addressed: dabaver65@hotmail.com

## I Introduction

Advanced divertor configurations such as the super-X divertor<sup>1</sup> are important for managing heat fluxes in the divertor region of present day and next-generation fusion experiments.<sup>2</sup> Modeling their behavior provides essential predictive capability for evaluating such designs. Of particular importance in this regard is the modeling of instabilities in the scrape-off layer and private flux region. These topological regions extend into the divertor leg, and therefore are likely to exhibit different behavior in different divertor configurations. Turbulence and filamentary structures in these regions can play an important role in distributing heat flux, and thus are essential to evaluating the performance of such designs.

Filaments in the private flux region, presumably generated by instabilities, have been observed in a number of experiments. Harrison<sup>3</sup> and Walkden<sup>4</sup> observed such instability in MAST. Scotti<sup>5</sup> observed filaments in the inner divertor leg of NSTX-U. Terry<sup>6</sup> also observed inner leg filaments in Alcator C-mod. In addition, this topic has been the focus of a number of theoretical<sup>7,8,9,10,11,12,13</sup> and experimental<sup>14</sup> studies.

An important tool for understanding such turbulence is the use of linear calculations. While such calculations do not model the saturation mechanism or energy cascade of such turbulence, they can provide insight into the underlying instability and associated mechanisms driving the turbulence. They also allow a detailed analysis of the role of specific terms in the model equations; once an eigenmode has been calculated, the resulting amplitudes can be substituted back into the model equations to determine their relative significance. This reveals the physical mechanism behind the turbulence. This type of analysis is difficult to perform on fully developed turbulence, hence illustrating the value of a linear simulation.

Linear instabilities in the scrape-off layer and private flux region have been considered in previous theoretical work. In Refs. 7 and 8 a dispersion relation was derived for low-beta flute-like modes in the divertor-leg region under the combined drives of curvature, sheath impedance and divertor plate tilt effects. More general geometry was treated in Ref. 9 which included the destabilizing contribution of geodesic curvature on flute modes. We will return to the role of geodesic curvature in detail later, as it is the main focus of our paper. A different instability, driven by sheath boundary conditions, the  $\nabla T_e$  sheath instability or so-called 'conducting wall' instability was considered in Ref. 10 and 11.

This paper describes a series of linear simulations of the private flux region of the MAST-Upgrade spherical tokamak plasma using design geometry and physical parameters. The simulations compare different models to determine which terms in the physics model are essential, and compare different divertor configurations to determine how they affect the eigenmodes. It then uses the calculated linear eigenmodes to determine what each term in the model is doing and why. This analysis reveals a feature of instability in the private flux region that, while mathematically well understood, is nonetheless physically counterintuitive.

## II Procedure

This is the author's peer reviewed, accepted manuscript. However, the online version of record will be different from this version once it has been copyedited and typeset.

PLEASE CITE THIS ARTICLE AS DOI: 10.1063/1.50063766

#### A. Simulation code

The computations in this article are performed using a code called ArbiTER.<sup>15</sup> This code is described in more detail in the references, but is summarized here for convenience.

The ArbiTER code is a linear eigenvalue code. That is to say, rather than simulating the evolution of plasma parameters through time, the code instead identifies dominant instability eigenmodes. This is done by first discretizing the model equations for a given set of magnetic and plasma profile data. This converts the model equations into matrix form, resulting in a generalized eigenvalue problem:

$$Ax = B\lambda x \quad (1)$$

From here the matrix equation is passed to the SLEPc<sup>16</sup> sparse eigensolver package. The resulting eigenvector is then mapped to the coordinate system of the original partial differential equations.

In addition to ArbiTER, a number of Mathematica scripts are used to set up profile data and to visualize output data.

An important property of this code for the purposes of the current study is that, rather than returning a comprehensive list of eigenmodes, it instead returns some specified number of eigenmodes that are selected to have the fastest growth rates. This is in part because it is based on a sparse eigenvalue solver, which unlike a full eigenvalue solver does not calculate all of the eigenvalues, but additionally because the number of eigenvalues is extremely high of which only a handful are of physical interest. In the current study the number of eigenmodes selected is ten, but this can be adjusted based on the needs of the problem. This is important as many of the features of this study are designed to regulate what kinds of instabilities make it into this top ten list. It should be understood that even without these features these eigenmodes are still valid solutions of the matrix equation and can still be calculated, but may not be returned as answers for a given set of run-time parameters. For this reason, special provisions must sometimes be made to ensure that eigenmodes of interest are not superseded by eigenmodes that are not the primary focus of the study.

#### B. Coordinate system

This study uses a type of quasi-ballooning coordinates. In this system, two different but related non-orthogonal coordinate systems are used: field-line following and geometric toroidal angle. The field-line following coordinates are used to calculate parallel derivatives, whereas the geometric angle coordinates are used to calculate perpendicular derivatives. This hybrid system allows the code to account for integrated magnetic shear without imposing a high radial resolution requirement.

The field line following coordinates are also used by BOUT<sup>17</sup> and by most of the turbulence models built under the BOUT++<sup>18</sup> framework. They are also used by the predecessor of ArbiTER, the 2DX code<sup>19</sup>. Field-line following coordinates as implemented here are discussed in greater detail in Sec. 3 of Ref. 18, or in Sec. 3 of Ref. 19. This coordinate system is defined by:

$$x = \psi - \psi_s \quad (2)$$

$$y = \theta \quad (3)$$

$$z = \zeta - \int_{\theta_0} d\theta \nu(\psi, \theta) \quad (4)$$

where  $\zeta$  is the toroidal angle,  $\theta$  is a poloidal angle variable,  $\psi$  is the poloidal flux, and  $\nu$  is the local safety factor. In the geometric toroidal angle coordinate system, one modification is made:

$$z' = \zeta \quad (5)$$

In both cases, toroidal symmetry allows the instability to be represented as a superposition of toroidal Fourier modes, that is to say, for an arbitrary perturbed quantity  $Q$ , we express  $Q = Q_o(x, y)e^{inz} = Q'_o(x, y)e^{inz'}$ , where  $n$  is the toroidal mode number, and  $Q_o$  and  $Q'_o$  are representations of the instability waveform in the field-line following and geometric angle coordinate systems, respectively. To interconvert between the two, the perturbed quantity is multiplied by an exponential  $e^{\pm inI}$ , where  $I = -\int_{\theta_0} d\theta \nu(\psi, \theta)$ .

In the context of the ArbiTER code, these two coordinate systems are combined by calculating the instability eigenfunction in the geometric angle representation, and re-defining the parallel derivative operators in order to convert to the field-line following coordinate system before calculating the parallel derivative and to convert back to geometric angle coordinates after calculating the derivative. This results in an operator of the form:

$$\partial_{\parallel QB} Q = e^{inI} \partial_{\parallel} e^{-inI} Q \quad (6)$$

where  $\partial_{\parallel} Q = \vec{B} \cdot \nabla(Q/B)$ .

These coordinates are used to define a number of geometric profile functions, in particular the binormal wavenumber  $k_b = -nB/|\nabla\psi|$  and the radial wavenumber  $k_\psi = -n\nu\nabla\theta \cdot \nabla\psi/|\nabla\psi|$ . These definitions are used throughout this paper.

### C. Model equations

In this study, three models are used. All of them are subsets of a 6-field Braginskii model<sup>17,20,21</sup> describing, among other phenomena, resistive and drift-resistive modes. There are a vast number of publications on resistive modes: two examples of early work employing similar equations are cited here.<sup>22,23</sup> Much of the early work is devoted to relatively less collisional plasmas on closed flux surfaces, where growth rates are typically small. More closely related to the present work is the fast resistive branch discussion by Novakovskii.<sup>24</sup>

The models considered in the present paper range from simple to more realistic, and by comparing these models it is possible to determine the level of physical realism needed to understand the principal dynamics of the plasma in the region of interest.

This is the author's peer reviewed, accepted manuscript. However, the online version of record will be different from this version once it has been copyedited and typeset.

PLEASE CITE THIS ARTICLE AS DOI: 10.1063/1.50063766

The simplest of these models is a 3-field resistive ballooning model.<sup>22,23,24</sup> Its model equations are as follows:

$$\gamma \nabla_{\perp}^2 \delta \phi = -\frac{B^2}{n_0} \partial_{\parallel} \nabla_{\perp}^2 \delta A + \frac{2B}{n_0} C_r \delta P \quad (7)$$

$$\gamma \delta n = -\delta v_E \cdot \nabla n_0 \quad (8)$$

$$-\gamma \nabla_{\perp}^2 \delta A + \gamma \frac{n}{\delta_{er}^2} \delta A = v_e \nabla_{\perp}^2 \delta A - \mu n \nabla_{\parallel} \delta \phi \quad (9)$$

where:

$$C_r \equiv \vec{b} \times \kappa \cdot \nabla \quad (10)$$

$$\delta v_E \cdot \nabla Q \equiv -i \frac{k_b (\partial_r Q)}{B} \delta \phi \quad (11)$$

$$v_E \cdot \nabla \delta Q \equiv -i \frac{k_b (\partial_r \phi)}{B} \delta Q \quad (12)$$

$$\delta b \cdot \nabla Q \equiv -i \frac{k_b (\partial_r A)}{\mu \delta_{er}^2 B} \delta Q \quad (13)$$

$$\delta P \equiv (T_i + T_e) \delta n + n_o \delta T_i + n_o \delta T_e \quad (14)$$

where  $\gamma$  is the eigenvalue to be determined,  $k_b$  is the binormal wavenumber,  $\mu$  is the ion/electron mass ratio,  $\delta_{er}$  is the skin depth, and  $Q$  is an arbitrary quantity.

This and the subsequent models use zero-value boundary conditions in the perpendicular direction, and sheath boundary conditions in the parallel direction. The sheath boundary condition is defined by:

$$\delta J_{\parallel} |_{bdry} = -s_n \frac{ne^2 c_s}{T_e} \delta \phi \quad (15)$$

where  $s_n = \mathbf{b} \cdot \mathbf{n} = \pm 1$ .

The next is a 3-field drift-ballooning model.<sup>17,20,25</sup> This contains additional terms to incorporate drift wave physics, but retains ballooning terms. These equations are as follows:

$$\gamma \nabla_{\perp}^2 \delta \phi = -\frac{B^2}{n_0} \partial_{\parallel} \nabla_{\perp}^2 \delta A + \frac{2B}{n_0} C_r \delta P \quad (16)$$

$$\gamma \delta n = -\delta v_E \cdot \nabla n_0 - \partial_{\parallel} \nabla_{\perp}^2 \delta A \quad (17)$$

$$-\gamma \nabla_{\perp}^2 \delta A + \gamma \frac{n}{\delta_{er}^2} \delta A = v_e \nabla_{\perp}^2 \delta A - \mu n \nabla_{\parallel} \delta \phi + \mu T_e \nabla_{\parallel} \delta n \quad (18)$$

The last model is a four-field model. It is based on a linearized subset of the STORM<sup>26</sup> turbulence model. This subset neglects terms related to parallel velocity, as it is assumed that growth rates exceed parallel flow rates, i.e.  $\gamma \gg k_{\parallel} c_s$ . These equations are as follows:

$$\gamma \nabla_{\perp}^2 \delta \phi = -\frac{B^2}{n_0} \partial_{\parallel} \nabla_{\perp}^2 \delta A + \frac{2B}{n_0} C_r \delta P \quad (19)$$

$$\gamma \delta n = -\delta v_E \cdot \nabla n_0 - \partial_{\parallel} \nabla_{\perp}^2 \delta A + \frac{2}{B} (C_r \delta P_e - n_0 C_r \delta \phi) \quad (20)$$

$$\begin{aligned} \gamma \delta T_e &= -\delta v_E \cdot \nabla T_e + \frac{2}{3} \partial_{\parallel} \chi_{\parallel} (\nabla_{\parallel} T_e + \delta b \cdot \nabla T_e) \\ &+ \frac{2(1.71)T_e}{3} \partial_{\parallel} \delta J + \frac{4T_e}{3B} \left( \frac{1}{n_0} C_r \delta P_e - C_r \delta \phi - \frac{5}{2} C_r \delta T_e \right) \end{aligned} \quad (21)$$

$$\begin{aligned} -\gamma \nabla_{\perp}^2 \delta A + \gamma \frac{n}{\delta_{er}^2} \delta A &= v_e \nabla_{\perp}^2 \delta A - \mu n \nabla_{\parallel} \delta \phi + \mu T_e \nabla_{\parallel} \delta n \\ &+ T_e \mu \delta b \cdot \nabla n_0 + 1.71 \mu n_0 \nabla_{\parallel} \delta T_e + 1.71 \mu n_0 \delta b \cdot \nabla T_e \end{aligned} \quad (22)$$

#### D. Numerical setup

The plasma profile functions and geometries used in this study are based on SOLPS<sup>27</sup> transport simulation models of MAST-U. Two magnetic geometries are used, one for a conventional divertor and one for a super-X divertor. These are shown in Fig. 1. From this magnetic geometry data, a number of important derived profiles are calculated. This includes poloidal flux ( $RB_p$ ), normal and geodesic curvature ( $\kappa_n, \kappa_v$ ), integrated magnetic shear ( $I$ ), and a variety of others.

Unlike the magnetic geometry, density and temperature profiles are modified from the original transport simulation data. These modifications take a number of forms. First, the profiles are chosen to be the same relative to the separatrix for both conventional and super-X configurations. This ensures an apples-to-apples comparison between the resulting instability eigenmodes and their growth rates. Second, the profiles have been flattened except in the private flux region. This allows the eigensolver to focus on instabilities existing in this region, so that modes in other regions do not displace the modes of interest from the top ten fastest growing eigenmodes. Third, the profiles are a parameter fit to a specified type of function rather than based on raw data; this ensures that the profiles are smooth enough to avoid spurious eigenmodes. Fourth, a cosh function rather than an exponential is used for fitting the density and electron temperature profiles; this ensures that the density and temperature gradients are nearly zero at the radial boundary, thus preventing modes from localizing at the simulation boundary where the effects of boundary conditions on the eigenmode could be unphysical. We note that experimental observations<sup>3-6</sup> have so far revealed modes that do not appear to connect to radial boundaries, motivating our choice. The results of these modifications are shown in Fig. 2.

An additional modification that is applied to some but not all of the runs is curvature masking. The purpose of this technique to suppress eigenmodes on the inner leg while having as little effect as possible on eigenmodes on the outer leg. This is accomplished by changing the curvature profile function (i.e. the pre-calculated curvature functions passed to the ArbiTER code, as opposed to the actual curvature of the magnetic geometry) to zero below a certain major radius  $R$ . This is applied to both normal and geodesic curvature, so it does not affect the relative importance of these terms. In the cases in this paper where curvature masking is applied, this is done by zeroing out curvature at a radius less than .55 m. Examples of this for a super-X divertor are shown in Fig. 3.

#### IV Numerical results

##### A. Comparison of models and instability types

The first matter to study is the types of eigenmodes that emerge from the above model equations under various circumstances. The cases being compared are distinguished by three considerations: 1) conventional vs. super-X divertors, 2) curvature masking vs. no curvature masking, and 3) choice of physics model, i.e. resistive ballooning, drift-ballooning, or the 4-field model. This results in a total of 12 different cases. Each of these is performed at a resolution of 128 grid points in both the  $x$  and  $y$  directions, and at a characteristic toroidal mode number of  $n=20$ . The eigensolver is set to return the top ten fastest growing eigenmodes. This results in a total of 120 eigenmodes to analyze.

The results of this study are summarized in Table 1. The first column is the case number, and the next three columns describe the parameters of the simulation, i.e. which model was used, which geometry was used, and whether curvature masking was in effect. The next two columns describe the locations of the ten fastest growing eigenmodes. The numbers in these columns give the order of the growth rate in the top ten list with 1 being the fastest. Eigenmodes localized to the inner divertor leg are listed in the inboard column, while eigenmodes localized to the outer divertor leg are listed in the outboard column. The last column then lists the most unstable eigenvalue in inverse seconds, with the imaginary part being the frequency.

From this table it is clear that the behavior of the three models is qualitatively similar. Quantitatively, there are some significant differences. In particular, the eigenvalues of the resistive ballooning model are distributed symmetrically with respect to frequency, whereas the eigenvalues from the other two models are not. This is shown in Fig. 4. From this it is apparent that resistive ballooning modes are replaced by drift or hybrid-drift modes in models where such modes are possible. However, the growth rates of the resulting modes are not qualitatively different, and do not significantly affect the ordering of the eigenmodes.

The similarity between the models is significant for two reasons. On one hand, the resistive ballooning model has curvature as its sole source of free energy. That it is able to replicate the results of the other two models implies that the dominant instabilities in this regime are predominantly curvature driven. On the other hand, the four-field model captures most of the essential physics of the linearized STORM model equations. This suggests that the results from this ensemble of runs contains eigenmodes that are present in STORM simulations,<sup>26</sup> and that are relevant to driving turbulence in that model.

The importance of curvature drive in these instabilities is complicated by two more patterns in this ensemble. First, the use of curvature masking is effective in removing all eigenmodes in the inner leg from the top ten list. This demonstrates that the inner leg modes are curvature-driven, which is not surprising since the inner leg private flux is in a bad curvature region. What is surprising is that there are outer leg modes available to take their place, regardless of the model equations used, despite the fact that the outer leg is in a good curvature region. That these modes are in fact localized to the outer leg can be confirmed by viewing their amplitudes in the R-Z plane, as is shown in Fig. 5.

The other pattern is that, in the super-X configuration, the outer leg modes are strong enough to make the top ten list even when curvature masking is absent. On one hand, this demonstrates an important difference between the behavior between the conventional and super-X divertors, thus making these results relevant to the comparison of these divertor types. On the other hand, it demonstrates that not only are outer leg modes present despite being in a good curvature region, but in fact are quite robust and able to compete with inner leg modes driven by bad curvature.

To resolve this conundrum, more detailed analysis of the structure of these eigenmodes and the underlying physics behind them follows.

#### B. Analysis of outer leg ballooning instability

To understand the mechanism behind the outer leg instabilities in the RBM model, it is necessary to move beyond generalizations such as “good curvature” and “bad curvature” and to look in detail at the mathematical structure of the curvature terms themselves.

The curvature term in Eq. 7 can be broken down into components. These components are given by the following equation:

$$C_r \equiv (k_b \kappa_n - k_\psi \kappa_g) - \text{Re}(i \kappa_g R B_p \partial_x) \equiv C_{rn} + C_{rg} + C_{rm} \quad (23)$$

where  $k_b$  is the binormal wavenumber,  $k_\psi$  is the radial wavenumber,  $\kappa_n \equiv \kappa \cdot \hat{e}_\psi$  is the normal curvature,  $\kappa_g \equiv \kappa \cdot \hat{b} \times \hat{e}_\psi$  is the geodesic curvature, and  $B_p$  is the poloidal field. For purposes of the definitions of geodesic and normal curvature,  $\hat{b}$  is the magnetic unit vector and  $\hat{e}_\psi$  is the flux surface normal.

In this framework, good or bad curvature corresponds to the sign of  $\kappa_n$  relative to the density gradient. The remaining terms are less intuitive. The value of  $k_\psi$  can be arbitrarily redefined by changing the location at which the integration of magnetic shear begins; this change in  $k_\psi$  is matched by an equal and opposite change in mode structure, which in this case affects the value of  $\partial_x$ . In quasi-ballooning coordinates this issue is avoided as component of  $k_\psi$  due to magnetic shear is set to zero, and instead  $k_\psi$  is determined by the degree of non-orthogonality in the computational grid. However, the mode structure is essentially arbitrary, so  $\text{Re}(i \kappa_g R B_p \partial_x)$  can potentially take either sign.

The actual value of  $C_{rm}$  can be calculated based on the calculated mode structure. In particular, since the curvature operator is applied to  $\delta n$  in Eqs. 7 and 16, one can write  $C_r \equiv C_r \delta n / \delta n$ , from which the value of  $C_{rm}$  can be calculated as  $\text{Re}(i \kappa_g R B_p \partial_x \ln(\delta n))$ . This allows all of the components of curvature, regardless of whether they depend on mode structure, to be compared on equal footing.

The results of this calculation are shown in Fig. 6. Here the three components of the curvature drive are compared, as well as their total. In this instance, the normal curvature term is positive near the eigenmode peak, which corresponds to good curvature. However, the contribution from mode structure, as well as the total, are both negative, i.e. destabilizing. The first part is not surprising given the orientation of the pressure gradient and toroidal curvature and the position of the mode within the divertor channel. However, it is still significant because it rules out a more conventional sort of curvature-driven instability, such as those described in Refs 7 and 8. The reversal of total curvature drive due to geodesic curvature is strongly dependent on radial mode structure. This implies that mode structure is critical to this type of instability, and also implies that it is not included in any model that does not account for radial mode structure.

An example of an eigenmode that displays this effect is shown in Fig. 7. In this figure, the real and imaginary parts of the eigenmode at a specific poloidal position are plotted versus flux surface. This shows a mode structure that is oblique with respect to the flux surface, i.e. plasma is being interchanged along an axis that is predominantly tangential rather than normal to the flux surface. The significance of this will become apparent in the discussion of theory.

#### C. Mode number scan

In order to ensure that the toroidal mode number produces a mode that is representative of turbulent behavior in the region of interest, a growth rate spectrum in toroidal mode number is needed.

Several such spectra are shown in Fig. 8. In the case of the conventional divertor with no curvature masking, this shows a characteristic "knee" around  $n=15$ . In all other cases, growth rates increase slowly with toroidal mode number. While results from the resistive ballooning model do not exhibit a toroidal mode number where the growth rate is maximized, they do exhibit a broad plateau in growth rates. Since  $n=20$  is clearly in this plateau for all cases considered, it is reasonable to take these results as typical for this type of instability in the region of interest. In reality, it is expected that the mode number spectra will maximize at a finite value of  $n$  beyond which ion diamagnetic drifts and dissipation start to dominate. These effects are difficult to model quantitatively in the divertor region without experimental data on neutral density and ion temperature; consequently, this has not been attempted here.

#### D. Convergence testing

In order to ensure that the computational grid has sufficient resolution in both the  $x$  and  $y$  directions, a convergence study was performed. This was done using an RBM case in super-X geometry with no curvature masking. This was chosen in order to observe the convergence of both inner and outer leg instabilities. Resolution was increased until further resolution produced no qualitative change in the distribution of eigenmodes, and then stopped at the previous value. These results are shown in Figs. 9.

These results show a threshold in  $y$  resolution above which the eigenmodes display mode twinning, i.e. for each eigenmode located in the upper divertor leg, there is a corresponding eigenmode in the lower divertor leg with a similar growth rate. The lack of this twinning at low resolution can be explained by the procedure by which the computational mesh is generated; grid points are chosen to be evenly spaced along the separatrix, however because the length of each region of the flux surface does not evenly divide the poloidal grid spacing,

grid points have different positions with respect to the upper x-point than the lower. At sufficiently high grid resolution, this difference is sufficiently small for mode twinning to occur. It therefore provides a convenient test of resolution adequacy.

In x resolution, the study shows that inner and outer leg modes converge at significantly different resolutions. This creates problems due to the fact that in the highest resolution cases, additional resolution is achieved by reducing the size of the domain and keeping the number of grid points fixed, rather than increasing the number of grid points. Because the outer leg modes are wider in radial extent than the inner leg modes, this means that the domains on which the inner leg modes are resolved are too narrow to simulate the outer leg modes. Since the modes of interest to this study are in the outer leg, a resolution suitable for convergence of outer leg modes was used despite the failure of outer leg modes to converge at this resolution.

## V Theoretical analysis

The presence of curvature driven ballooning modes in regions of good curvature may at first seem counterintuitive, but in fact this is predicted by established stability theory. The importance of geodesic curvature is noted by Coppi,<sup>28</sup> as far back as 1966 and its role has been discussed in later works.<sup>29,30,31</sup>

With the exception of Refs. 9 and 31 the earlier works consider closed surface edge plasmas which are relatively less collisional than considered here. As a result, modes are greatly extended along the field lines, wrapping poloidally many times around the torus. A two-scale analysis in the extended ballooning coordinate is usually performed. In Ref. 31 flute modes subject to sheath boundary conditions on a limiter in the scrape-off layer are considered in a model geometry where the geodesic curvature effects provide the drive because the normal curvature averages to zero.

Because the situation we consider here is quite different from those previous studies, it is helpful to review the underlying mechanism of these geodesic curvature instabilities in a concise manner that is relevant to the current modes of interest. The destabilizing contribution of geodesic curvature on flute modes in the private flux region was contained in Eq. (16) of Ref. 9, although the mechanism was not discussed in detail there.

The mechanism behind these modes can be understood by looking at a simpler problem, that of MHD instability in slab geometry in the local eikonal limit. In this case, the mode structure can be reduced to a sinusoidal function with a definite wavevector  $k$ . This can be described by the following dimensionless equations:

$$\gamma \nabla_{\perp}^2 \delta \phi = \frac{2B}{n_0} \mathbf{b} \times \kappa \cdot \nabla \delta P \quad (24)$$

$$\gamma \delta n = -i \delta \phi (\mathbf{b} \times \mathbf{k} \cdot \nabla n) \quad (25)$$

For the cold ion case with isothermal  $T_e$ , this yields the formula for  $\gamma$ :

$$\gamma^2 = \frac{2B}{n_0} \frac{(\mathbf{b} \times \mathbf{k} \cdot \kappa)(\mathbf{b} \times \mathbf{k} \cdot \nabla n)}{k_{\perp}^2} \quad (26)$$

Note that in this equation only the component of wavenumber perpendicular to the magnetic field matters. This corresponds to the two degrees of freedom in Eq. 23, one from the

toroidal mode number, which determines  $k_b$  and  $k_\psi$ , and one from the eigenmode structure in the radial (i.e.  $\mathbf{e}_\psi$ ) direction.

This growth rate is maximized over the orientation of  $\mathbf{k}$  when the term  $F \equiv (\mathbf{b} \times \mathbf{k} \cdot \kappa)(\mathbf{b} \times \mathbf{k} \cdot \nabla n)$  is maximized. To calculate when this will occur, let  $\mathbf{q} = \mathbf{b} \times \mathbf{k}/|\mathbf{b} \times \mathbf{k}|$ . Then the above term can be rewritten as:

$$F = (\mathbf{q} \cdot \mathbf{e}_R)(\mathbf{q} \cdot \mathbf{e}_\psi) \quad (27)$$

where  $\kappa \propto -\mathbf{e}_R$  and  $-\nabla P \propto \mathbf{e}_\psi = e_R \cos \theta + e_z \sin \theta$ . Now let  $\mathbf{q} = e_R \cos \varphi + e_z \sin \varphi$ . In this case,

$$F = \cos \varphi (\cos \varphi \cos \theta + \sin \varphi \sin \theta) = \cos \varphi \cos(\varphi - \theta) \quad (28)$$

which is maximized when:

$$\varphi = \theta/2 \quad (29)$$

This result has several implications. The first is that, except in the case of perfect good curvature where  $\theta = 0$ , there will always be a possibility of curvature-driven instability. The second is that, the further a flux surface is from perfect good curvature, the stronger the instability drive will be. The third is that, in order to exploit this instability drive, the wavenumber must be at an angle to the flux surface tangent.

All of these implications are evident in the instabilities observed here. First, an instability is observed regardless of good or bad curvature. Second, the instability is stronger in the super-X divertor, where flux surfaces are nearly horizontal and therefore the flux surface normal vector is nearly perpendicular to the curvature vector. Third, the eigenmode has an oblique structure, as shown in Fig. 7. Thus, despite their counterintuitive appearance, these instabilities are behaving exactly as analytic theory predicts.

## VI Conclusions

In the present paper, the stability of the private scrape off layer in the divertor legs of two different spherical tokamak configurations is examined using three physics models. This reveals the presence of a curvature-driven instability in the private flux region of the outer divertor leg. This instability is driven by geodesic rather than normal curvature, allowing it to exist in what is conventionally considered a good curvature region. The nature of this mode is revealed both by comparison of different models and test cases, as well as by detailed analysis of its underlying mode structure. This reveals an instability that, despite its initially paradoxical appearance, is readily explained by analytic theory.

The presence of this instability is particularly noteworthy given that it is significantly stronger in a super-X divertor than in a conventional divertor. This makes this instability important with respect to possible implications for the heat flux widths of these divertor types, in particular indicating that the super-X divertor may spread out divertor heat flux not only due to the effect of magnetic geometry, but also its effect on scrape-off layer stability. The presence of this effect suggests that geodesic curvature driven modes should be taken into account in future comparisons of advanced divertor designs. This also has implications for the designs

This is the author's peer reviewed, accepted manuscript. However, the online version of record will be different from this version once it has been copyedited and typeset.

PLEASE CITE THIS ARTICLE AS DOI: 10.1063/1.50063766

themselves, as it suggests that heat flux width might depend not only on flux expansion, but also on the orientation of the flux surface along its path to the divertor plate.

#### Acknowledgements

The authors have benefited a great deal from the contributions of their collaborators. In particular, we wish to thank Fabio Riva.

This material is based upon work supported by the U.S. Department of Energy Office of Science, Office of Fusion Energy Sciences under Award Number DE-SC0019270; however, such support does not constitute an endorsement by the DOE of the views expressed herein. It is also partially funded by the RCUK Energy Programme (grant no. EP/T012250/1).

#### Data Availability

The data in this article is openly available at <https://doi.org/10.5281/zenodo.5111014>.<sup>32</sup>

**Figures**

ab cd

Figure 1: Sample magnetic flux surfaces for the conventional divertor configuration (a) and corresponding SOLPS grid (b), and super-X configuration (c) and SOLPS grid (d). [Associated dataset available at <https://doi.org/10.5281/zenodo.5111014>]<sup>32</sup>

a  
b  
c

Figure 2: Density (a), electron temperature (b), and ion temperature (c) profiles. [Associated dataset available at <https://doi.org/10.5281/zenodo.5111014>]<sup>32</sup>

a b

Figure 3: Normal curvature in R-Z coordinates for a super-X divertor without (a) and with (b) curvature masking. [Associated dataset available at <https://doi.org/10.5281/zenodo.5111014>]<sup>32</sup>

Case	Model	Geometry	Masking	Inboard	Outboard	Leading eigenvalue ( $s^{-1}$ )
1	RBM	super-X	no	1-4,7-8	5-6,9-10	78131.5 - 35.3525 I
2	RDW	super-X	no	1-6,9	7-8,10	90015.8 - 6697.16 I
3	4 field	super-X	no	1-6,8	7,9	90281.6 - 17206.8 I
4	RBM	conventional	no	1-10		92269.7 + 22.4386 I
5	RDW	conventional	no	1-10		104227. - 5664.43 I
6	4 field	conventional	no	1-10		102849. - 16784.4 I
7	RBM	super-X	yes		1-10	64820.8 - 6231.77 I
8	RDW	super-X	yes		1-10	64434.1 + 2283.01 I
9	4 field	super-X	yes		1-10	65677. - 1358.07 I
10	RBM	conventional	yes		1-10	25980.7 + 520.565 I
11	RDW	conventional	yes		1-10	34907.5 - 4975.13 I
12	4 field	conventional	yes		1-10	36149.5 - 10330.7 I

Table 1: physical locations of eigenmodes for a complete set of models and grids.

a) curvature masking, conventional b) no masking, super-X

Figure 4: Distribution of eigenvalues for two different runs in the parameter scan. [Associated dataset available at <https://doi.org/10.5281/zenodo.5111014>]<sup>32</sup>

This is the author's peer reviewed, accepted manuscript. However, the online version of record will be different from this version once it has been copyedited and typeset.

PLEASE CITE THIS ARTICLE AS DOI: 10.1063/1.50063766

a b

Figure 5: location of eigenmodes in RZ coordinates, for RBM super-X no masking, mode 5 (a) and for RBM conventional with masking, mode 1 (b). [Associated dataset available at <https://doi.org/10.5281/zenodo.5111014>]<sup>32</sup>

Figure 6: Curvature drive term as a function of distance in the R-Z plane along the flux surface of the mode peak for the eigenmode in Fig. 5a, with negative values destabilizing. [Associated dataset available at <https://doi.org/10.5281/zenodo.5111014>]<sup>32</sup>

Figure 7: Radial mode structure of density fluctuations for eigenmode in Fig. 5a as a function of distance in the R-Z plane at the poloidal position of the mode peak. [Associated dataset available at <https://doi.org/10.5281/zenodo.5111014>]<sup>32</sup>

Figure 8: growth rate as a function of toroidal mode number for a number of cases. [Associated dataset available at <https://doi.org/10.5281/zenodo.5111014>]<sup>32</sup>

scan in y resolution scan in x resolution

Figure 9: convergence testing. Red points indicate inboard localized modes, blue points indicate outboard localized modes. Note that for x resolutions over 512 the listed resolution is the effective resolution at the original domain size, whereas the actual domain size is reduced. [Associated dataset available at <https://doi.org/10.5281/zenodo.5111014>]<sup>32</sup>

This is the author's peer reviewed, accepted manuscript. However, the online version of record will be different from this version once it has been copyedited and typeset.

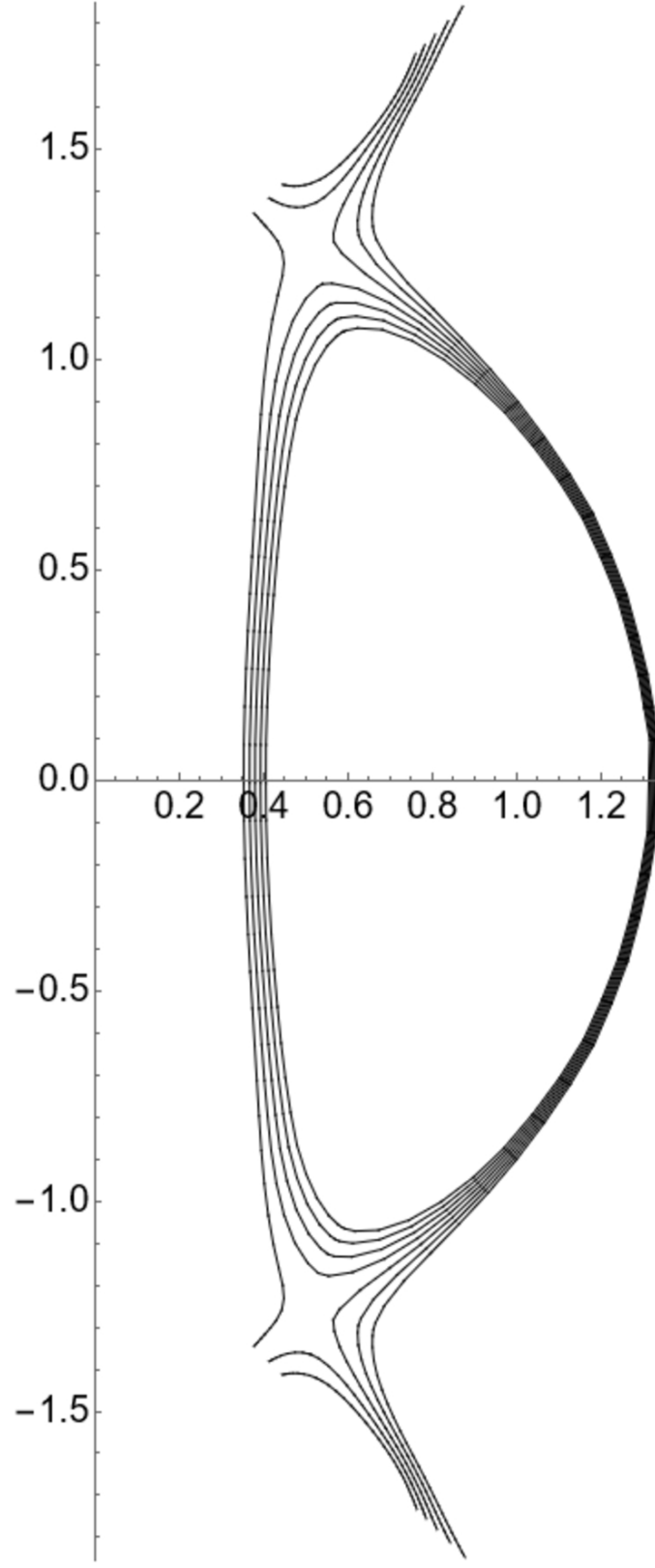
PLEASE CITE THIS ARTICLE AS DOI: 10.1063/5.0063766

## References

- <sup>1</sup> P. M. Valanju, M. Kotschenreuther, S. M. Mahajan, J. Canik, *Phys. Plasmas* **16**, 056110 (2019).
- <sup>2</sup> T. Eich, A. W. Leonard, R. A. Pitts, W. Fundamenski, R. J. Goldston, T. K. Gray, A. Herrmann, A. Kirk, A. Kallenbach, O. Kardaun *et al*, *Nucl. Fusion* **53**, 093031 (2013).
- <sup>3</sup> J. R. Harrison, G. M. Fishpool, A. J. Thornton, N. R. Walkden, and MAST team, *Phys. Plasmas* **22**, 092508 (2015).
- <sup>4</sup> N.R. Walkden, J. Harrison, S.A. Silburn, T. Farley, S.S. Henderson, A. Kirk, F. Militello, A. Thornton and The MAST Team, *Nucl. Fusion* **57**, 126028 (2017).
- <sup>5</sup> F. Scotti, S. Zweben, V. Soukhanovskii, D. Baver and J. Myra, *Nucl. Fusion* **58**, 126028 (2018).
- <sup>6</sup> J.L. Terry, S. Ballinger, D. Brunner, B. LaBombard, A.E. White, S.J. Zweben, *Nucl. Mater. Energy* **12**, 989 (2017).
- <sup>7</sup> R. H. Cohen and D. D. Ryutov, *Contrib. Plasma Phys.* **46**, 678 (2006).
- <sup>8</sup> R. H. Cohen, B. LaBombard, D. D. Ryutov, J. L. Terry, M. V. Umansky, X. Q. Xu, and S. Zweben, *Nucl. Fusion* **47**, 612 (2007).
- <sup>9</sup> D. D. Ryutov and R. H. Cohen, *Contrib. Plasma Phys.* **48**, 48 (2008).
- <sup>10</sup> D. D. Ryutov and R. H. Cohen, *Contrib. Plasma Phys.* **44**, 168 (2004).
- <sup>11</sup> R. H. Cohen and D. D. Ryutov, *Plasma Phys. Controlled Fusion* **47**, 1187 (2005).
- <sup>12</sup> M. Giacomini, L. N. Stenger, and P. Ricci, *Nucl. Fusion* **60**, 024001 (2020).
- <sup>13</sup> S. Baschetti, H. Bufferand, G. Ciraolo, Ph. Ghendrih, E. Serre, P. Tamain and the WEST Team, *Nucl. Fusion* **61**, 106020 (2021).
- <sup>14</sup> R. D. Nem, P. Manz, J. Juul Rasmussen, N. Vianello, N. Walkden, V. Naulin, B. Sieglin, A. Hermann, D. Brida, and the ASDEX Upgrade Team, *Plasma Phys. Controlled Fusion* **63**, 065005 (2021).
- <sup>15</sup> D. A. Baver, J. R. Myra and M. V. Umansky, *Commun. Comp. Phys.* **20**, 136 (2016).
- <sup>16</sup> <http://www.grycap.upv.es/slepc>
- <sup>17</sup> M. V. Umansky, X. Q. Xu, B. Dudson, L. L. LoDestro, J. R. Myra, *Computer Phys. Comm.* **180**, 887 (2009).
- <sup>18</sup> B. D. Dudson, M. V. Umansky, X. Q. Xu, P. B. Snyder, H. R. Wilson, *Computer Physics Communications* **180**, 1467 (2009).
- <sup>19</sup> D. A. Baver, J. R. Myra, and M. V. Umansky, *Comp. Phys. Comm.* **182**, 1610 (2011).
- <sup>20</sup> P. J. Catto, A. N. Simakov, *Phys. Plasmas* **11** (2004) 2326.
- <sup>21</sup> S. I. Braginskii, "Transport processes in a plasma", *Reviews of Plasma Physics* (Leontovich, M.A., Ed.), Vol. 1, Consultants Bureau, New York (1965) 205.
- <sup>22</sup> P. H. Diamond, P. L. Similon, T. C. Hender and B. A. Carreras, *Phys. Fluids* **28**, 1116 (1985).
- <sup>23</sup> J. F. Drake and T. M. Antonsen Jr, *Phys. Fluids* **28**, 544 (1985).
- <sup>24</sup> S. V. Novakovskii, P. N. Guzdar, J. F. Drake, C. S. Liu, and F. L. Waelbroeck, *Phys. Plasmas* **2**, 781 (1995).
- <sup>25</sup> A. Zeiler, D. Biskamp, J. F. Drake and P. N. Guzdar, *Phys. Plasmas* **3**, 2951 (1996).
- <sup>26</sup> Fabio Riva, Fulvio Militello, Sarah Elmore, John T. Omotani, Ben Dudson, Nick R. Walkden, and the MAST team, *Plasma Phys. Control. Fus.* **61**, 095013 (2019).
- <sup>27</sup> Moulton D, Lipschultz B, Harrison J, Detachment onset in MAST-U according to SOLPS-ITER, 44th EPS Conference on Plasma Physics, EPS 2017.
- <sup>28</sup> B. Coppi, *Nucl. Fusion* **6**, 293 (1966).
- <sup>29</sup> T. C. Hender, B. A. Carreras, W. A. Cooper, J. A. Holmes, P. H. Diamond and P. L. Similon, *Phys. Fluids* **27**, 1439 (1984).
- <sup>30</sup> R. J. Hastie, J. J. Ramos and F. Porcelli, *Phys. Plasmas* **10**, 4405 (2003).
- <sup>31</sup> S. V. Novakovskii, P. N. Guzdar, J. F. Drake, and C. S. Liu, *Physics of Plasmas* **2**, 3764 (1995).
- <sup>32</sup> Baver, D. A. (2021). Comparison of private scrape-off layer instability in conventional and super-X divertor configurations. <https://doi.org/10.5281/zenodo.5111014>

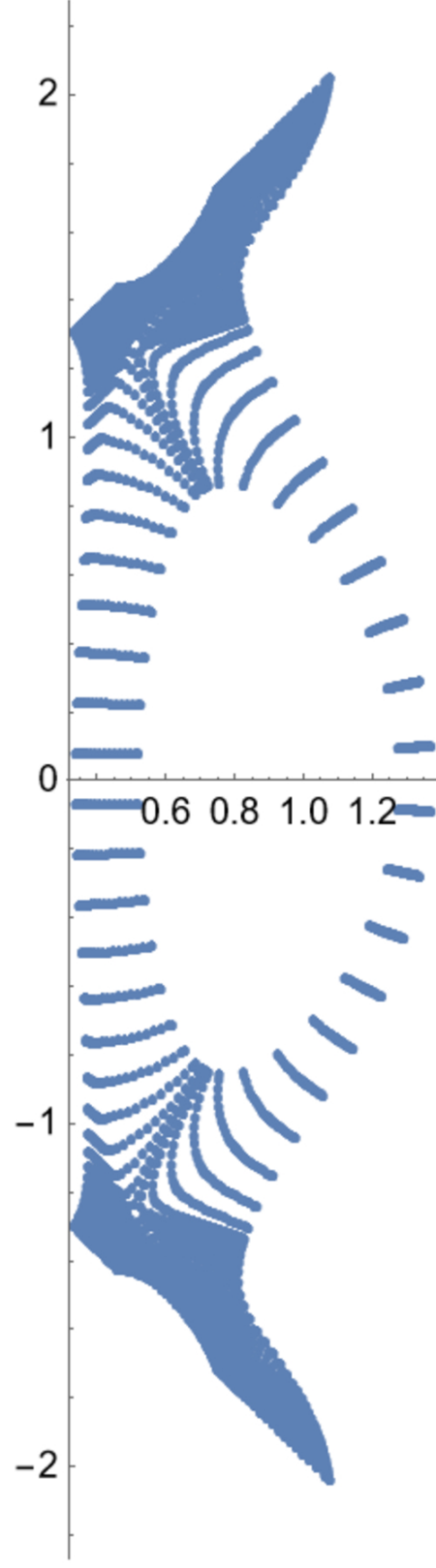
This is the author's peer reviewed, accepted manuscript. However, the online version of record will be different from this version once it has been copyedited and typeset.

PLEASE CITE THIS ARTICLE AS DOI: 10.1063/5.0063766



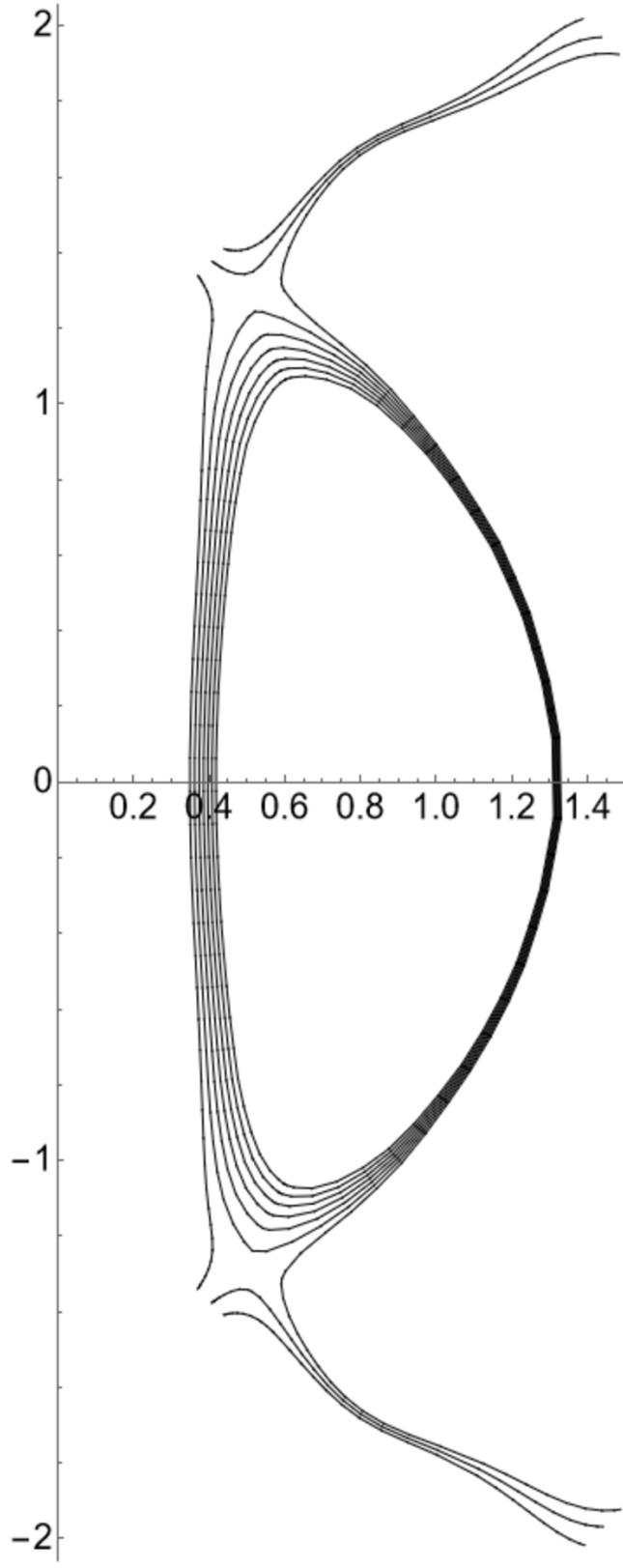
This is the author's peer reviewed, accepted manuscript. However, the online version of record will be different from this version once it has been copyedited and typeset.

PLEASE CITE THIS ARTICLE AS DOI: 10.1063/5.0063766



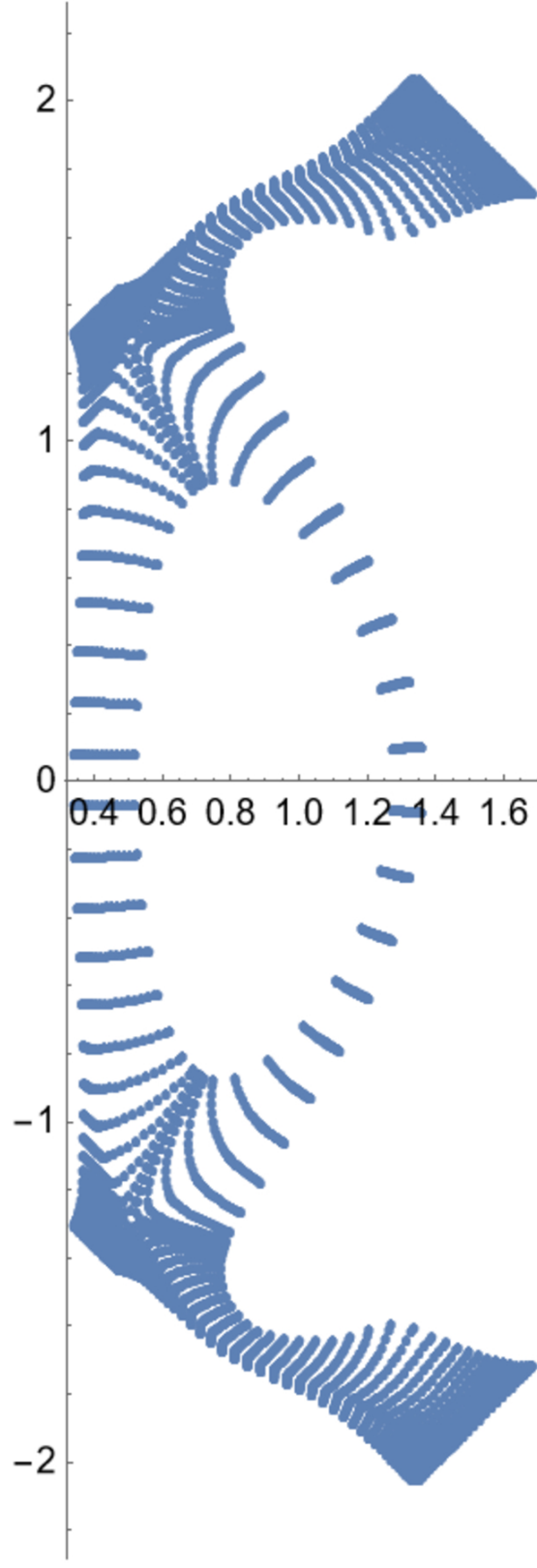
This is the author's peer reviewed, accepted manuscript. However, the online version of record will be different from this version once it has been copyedited and typeset.

PLEASE CITE THIS ARTICLE AS DOI: 10.1063/5.0063766



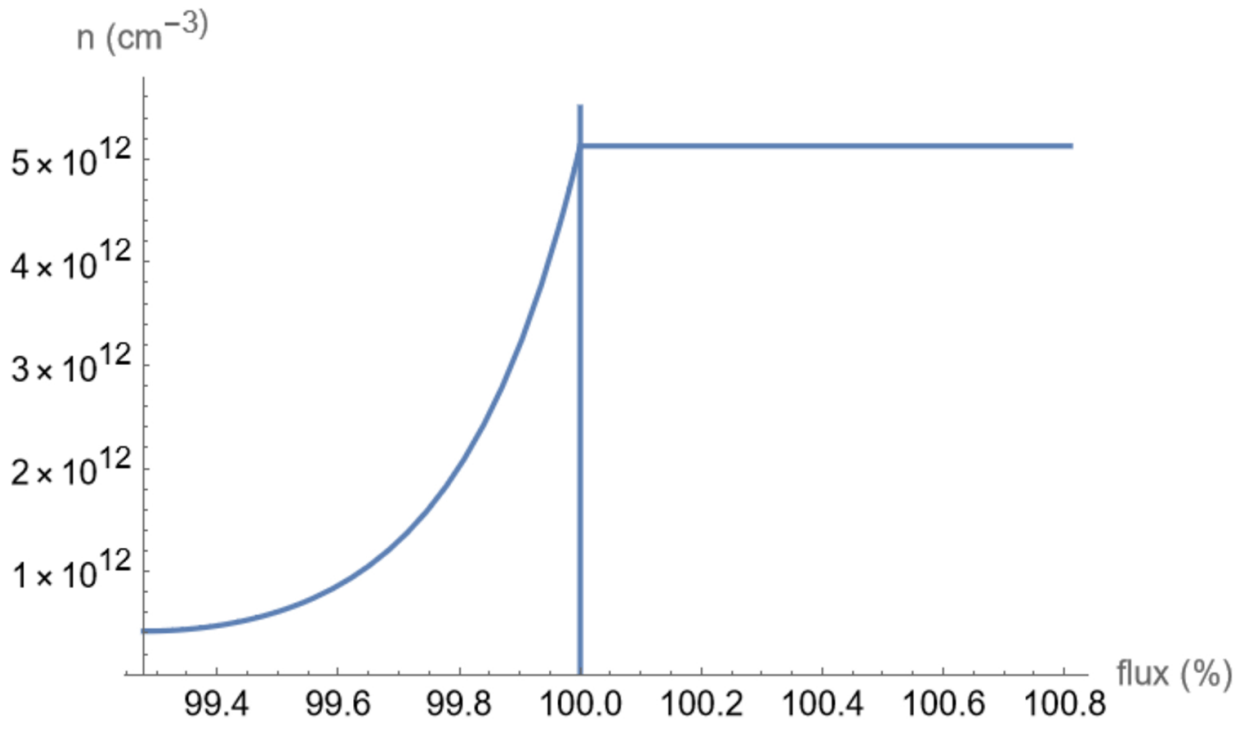
This is the author's peer reviewed, accepted manuscript. However, the online version of record will be different from this version once it has been copyedited and typeset.

PLEASE CITE THIS ARTICLE AS DOI: 10.1063/5.0063766



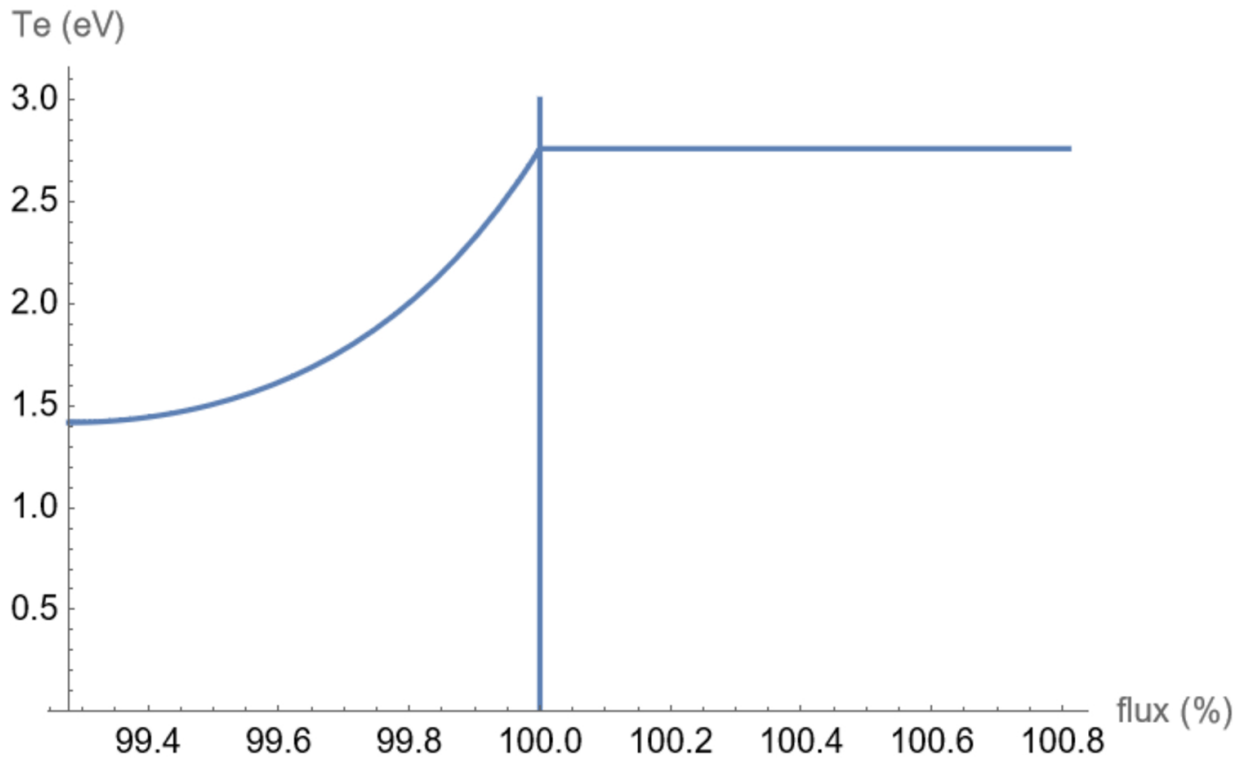
This is the author's peer reviewed, accepted manuscript. However, the online version of record will be different from this version once it has been copyedited and typeset.

PLEASE CITE THIS ARTICLE AS DOI: 10.1063/5.0063766



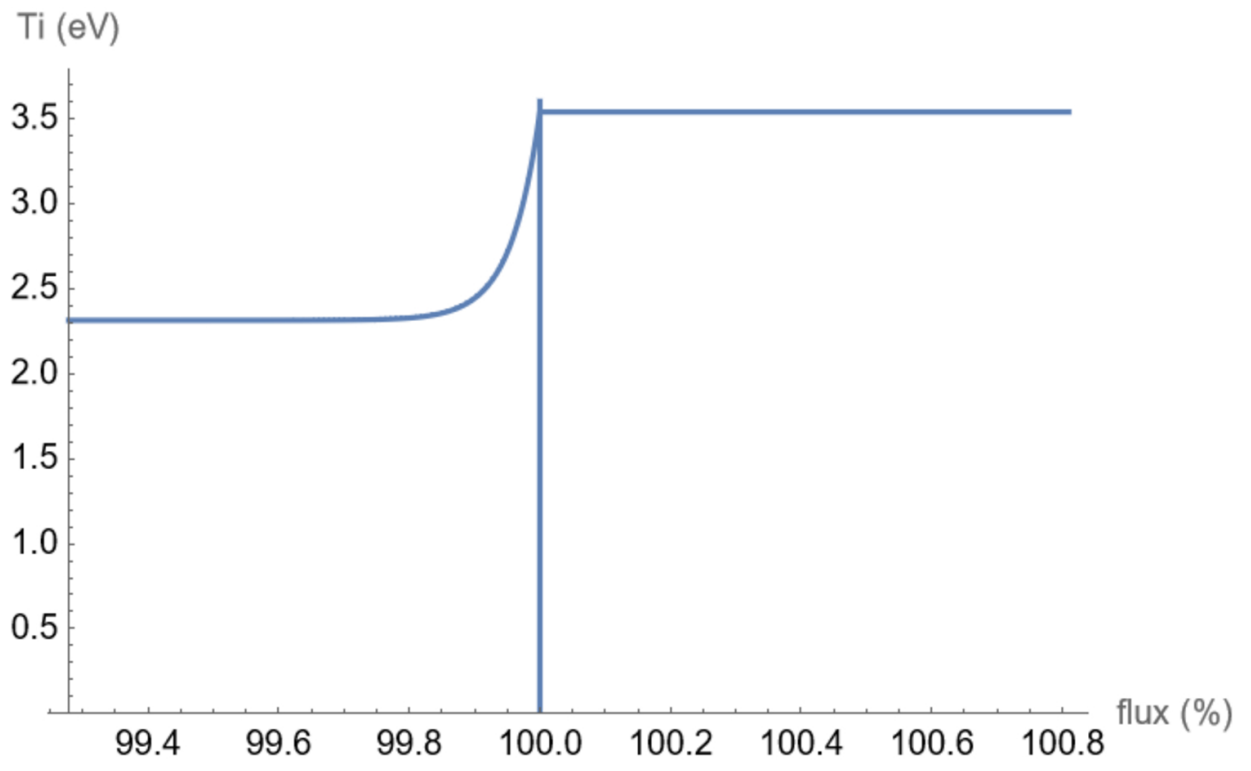
This is the author's peer reviewed, accepted manuscript. However, the online version of record will be different from this version once it has been copyedited and typeset.

PLEASE CITE THIS ARTICLE AS DOI: 10.1063/5.0063766



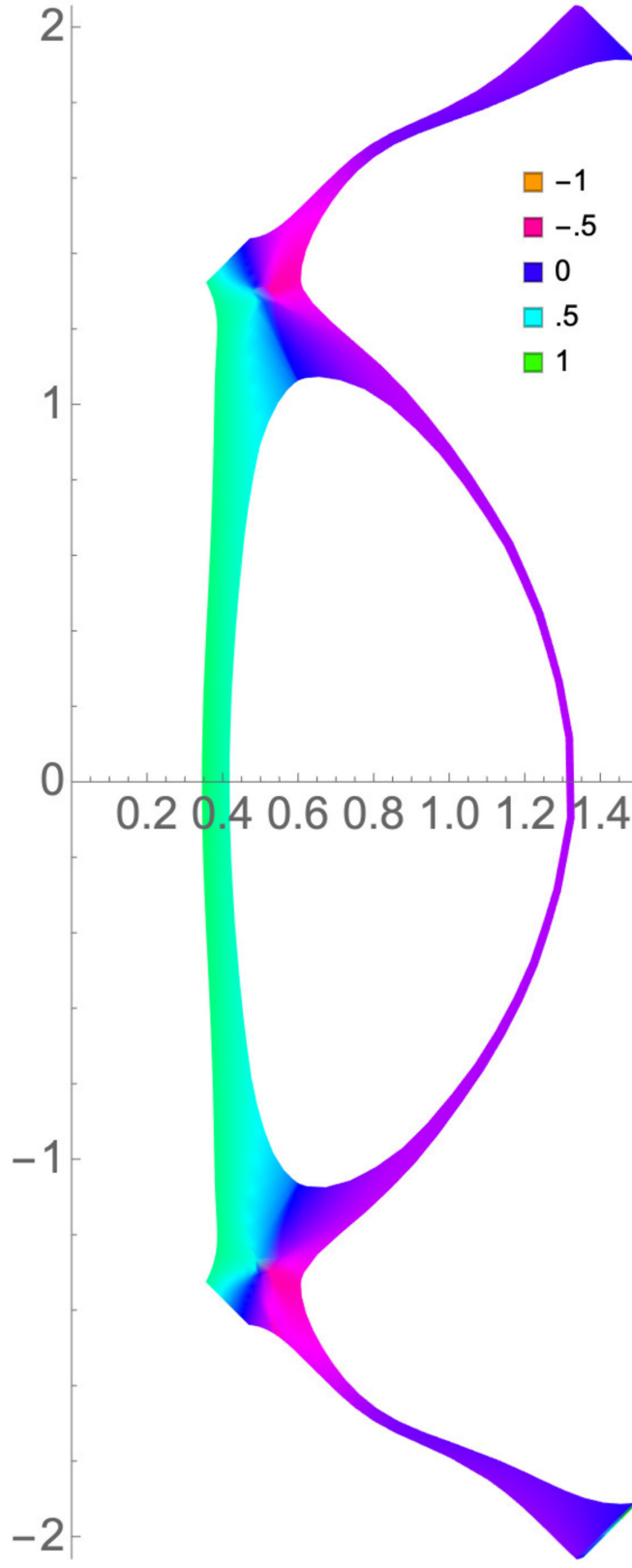
This is the author's peer reviewed, accepted manuscript. However, the online version of record will be different from this version once it has been copyedited and typeset.

PLEASE CITE THIS ARTICLE AS DOI: 10.1063/5.0063766

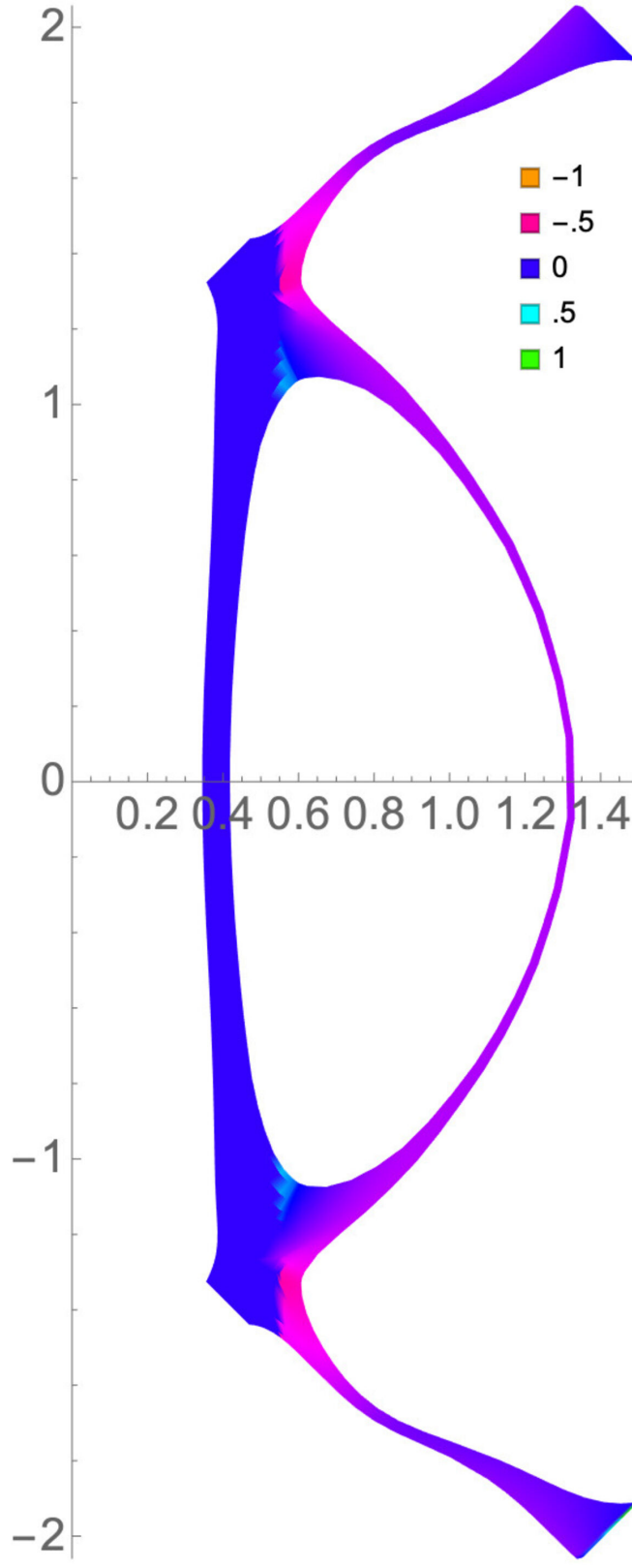


This is the author's peer reviewed, accepted manuscript. However, the online version of record will be different from this version once it has been copyedited and typeset.

PLEASE CITE THIS ARTICLE AS DOI: 10.1063/5.0063766

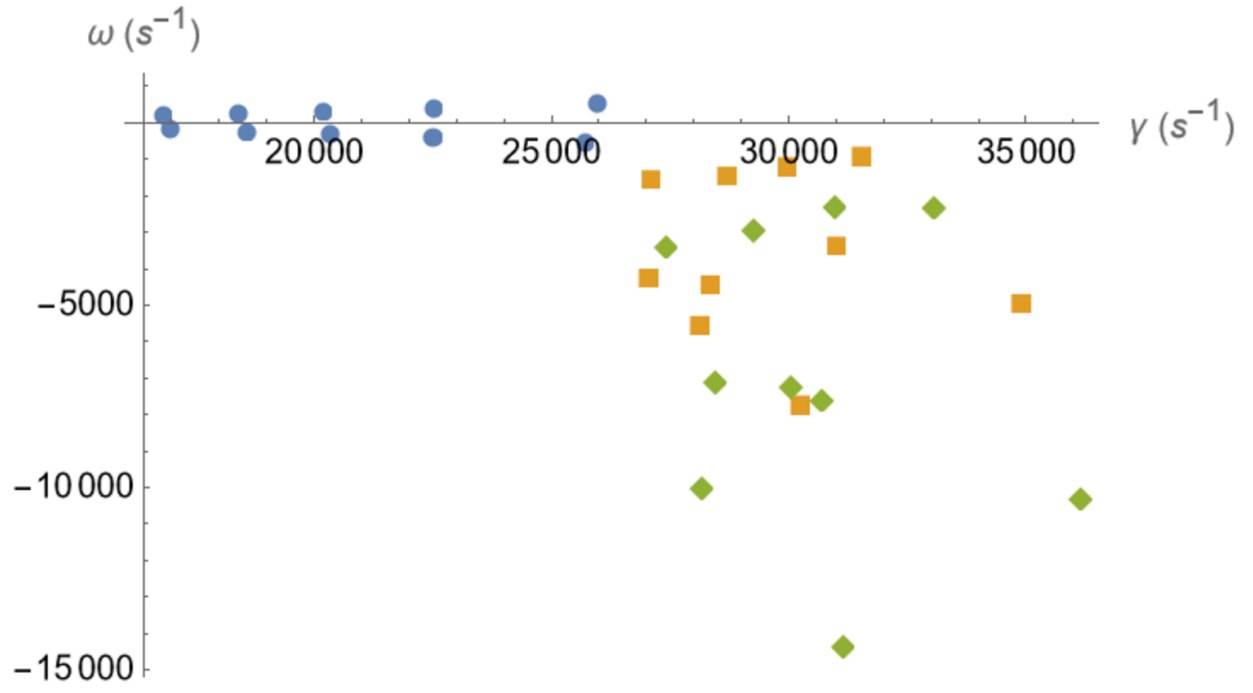


This is the author's peer reviewed, accepted manuscript. However, the online version of record will be different from this version once it has been copyedited and typeset.  
PLEASE CITE THIS ARTICLE AS DOI: 10.1063/5.0063766



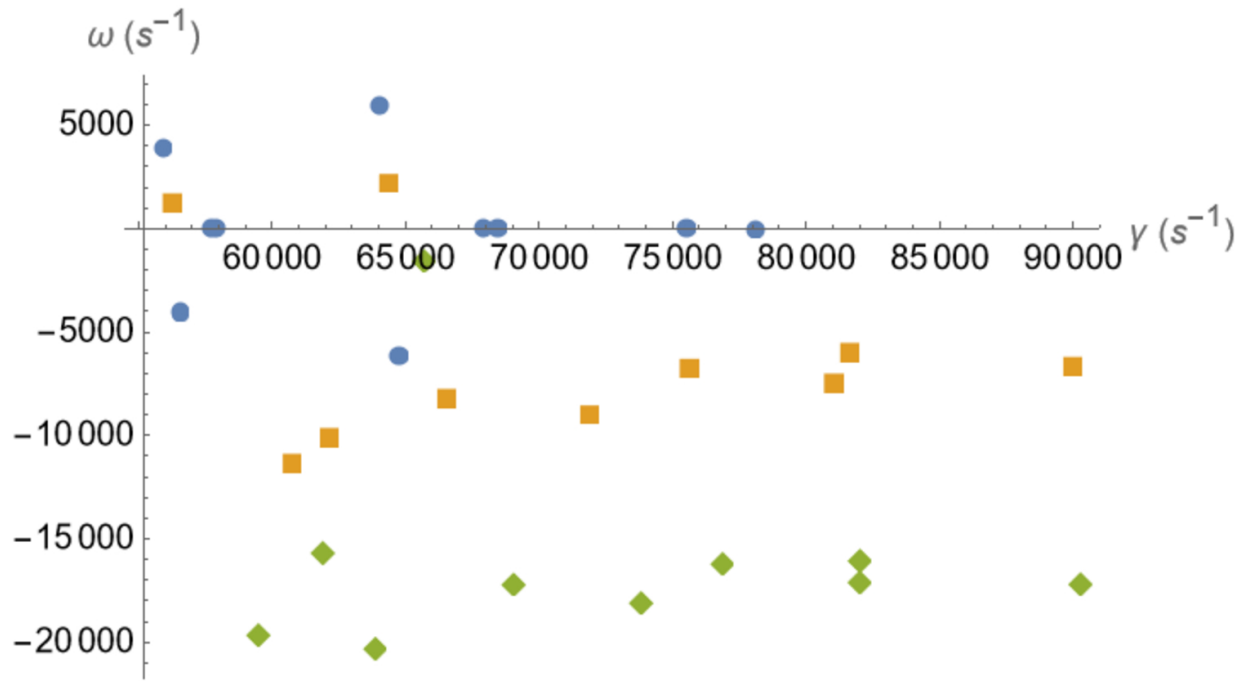
This is the author's peer reviewed, accepted manuscript. However, the online version of record will be different from this version once it has been copyedited and typeset.

PLEASE CITE THIS ARTICLE AS DOI: 10.1063/5.0063766



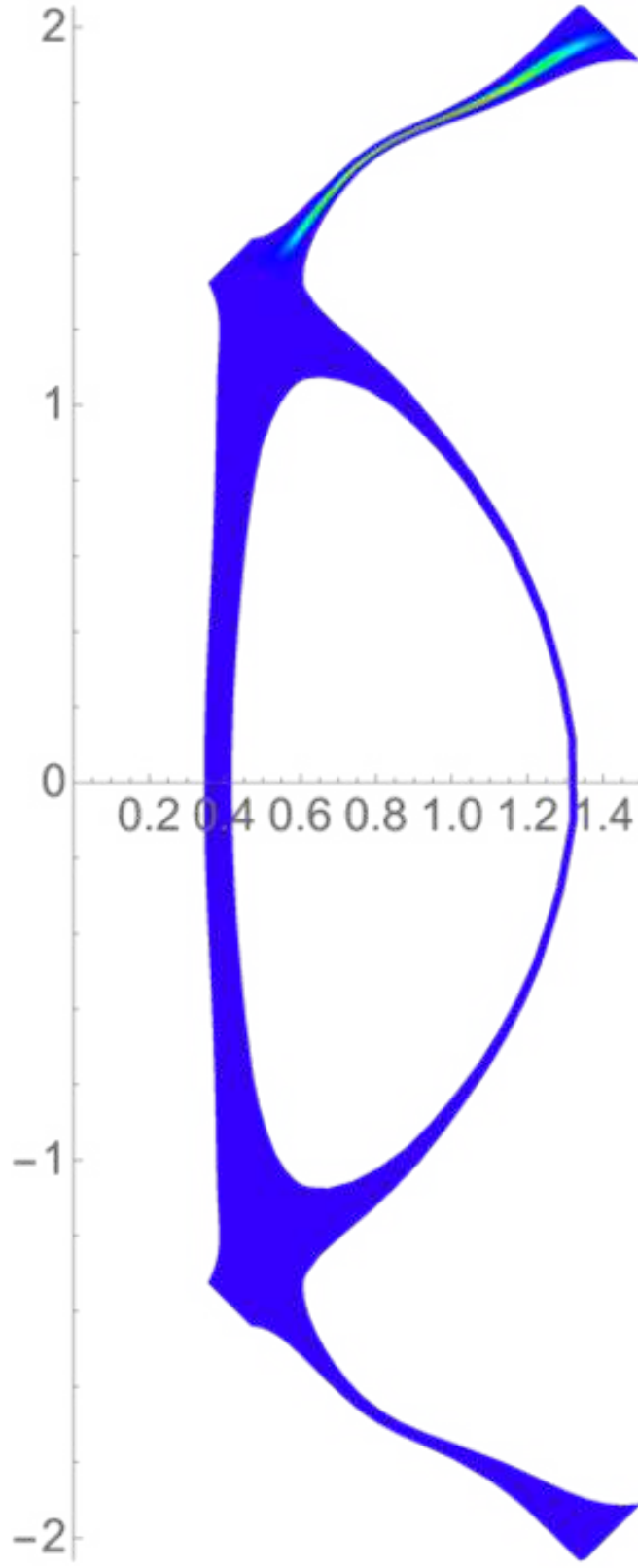
This is the author's peer reviewed, accepted manuscript. However, the online version of record will be different from this version once it has been copyedited and typeset.

PLEASE CITE THIS ARTICLE AS DOI: 10.1063/1.50063766



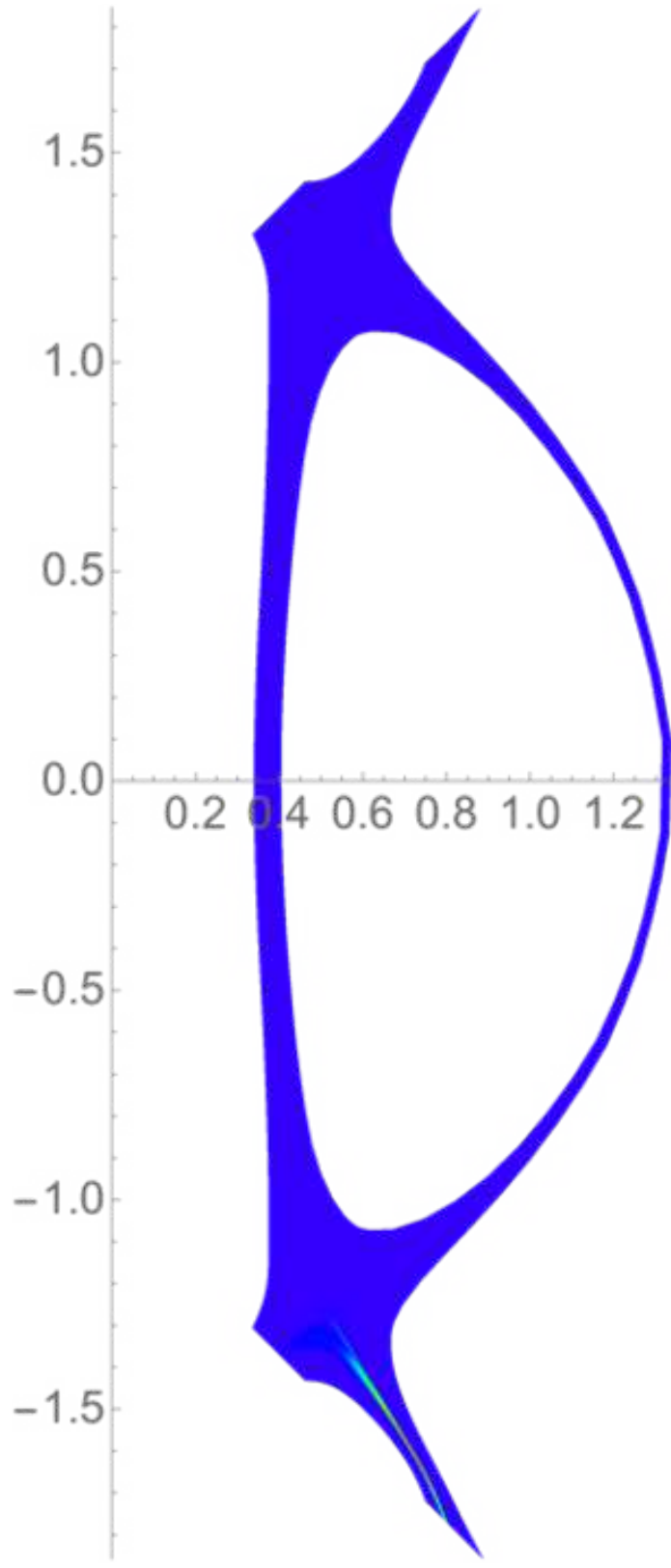
This is the author's peer reviewed, accepted manuscript. However, the online version of record will be different from this version once it has been copyedited and typeset.

PLEASE CITE THIS ARTICLE AS DOI: 10.1063/5.0063766



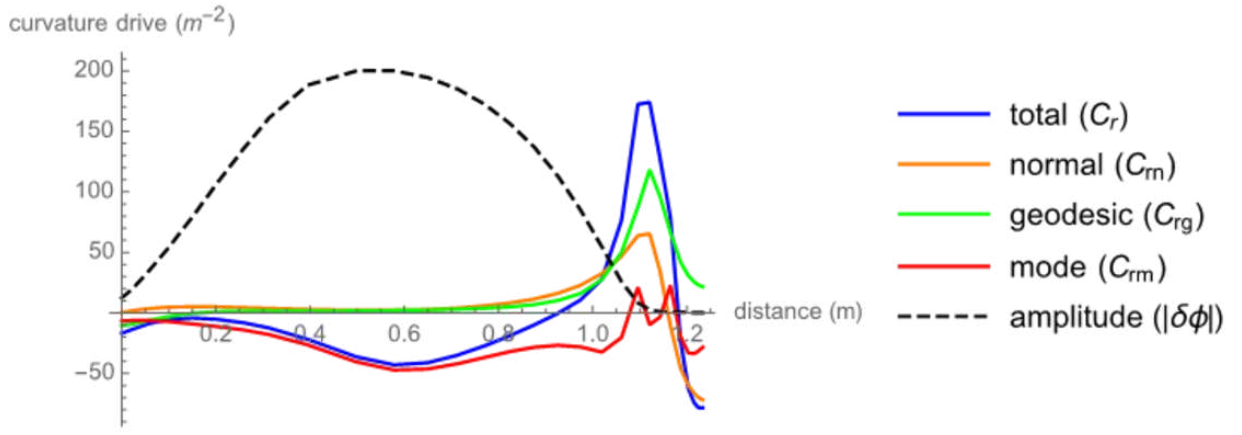
This is the author's peer reviewed, accepted manuscript. However, the online version of record will be different from this version once it has been copyedited and typeset.

PLEASE CITE THIS ARTICLE AS DOI: 10.1063/5.0063766



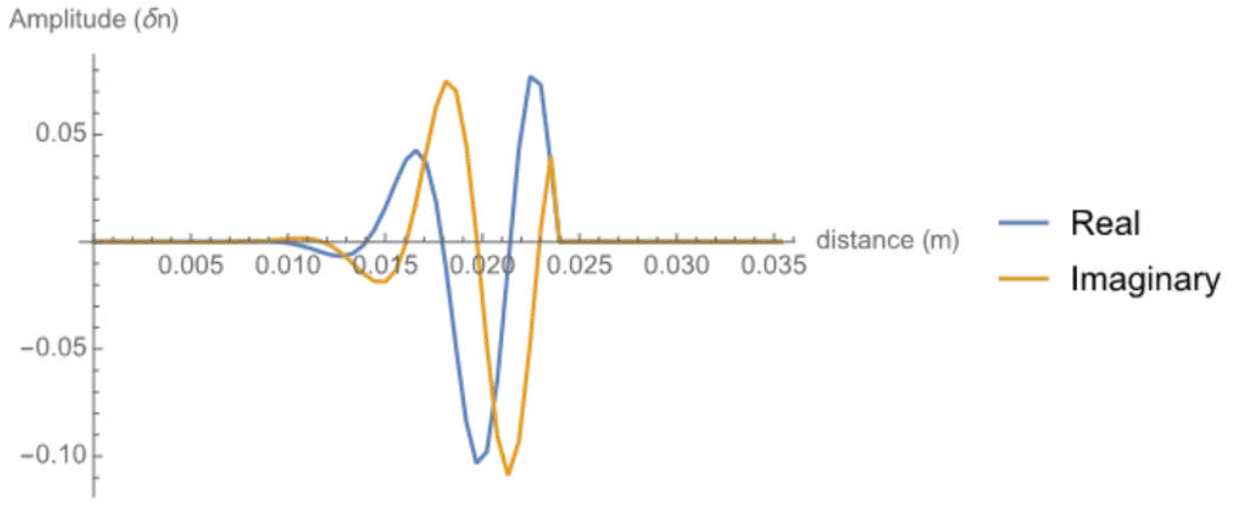
This is the author's peer reviewed, accepted manuscript. However, the online version of record will be different from this version once it has been copyedited and typeset.

PLEASE CITE THIS ARTICLE AS DOI: 10.1063/1.50063766



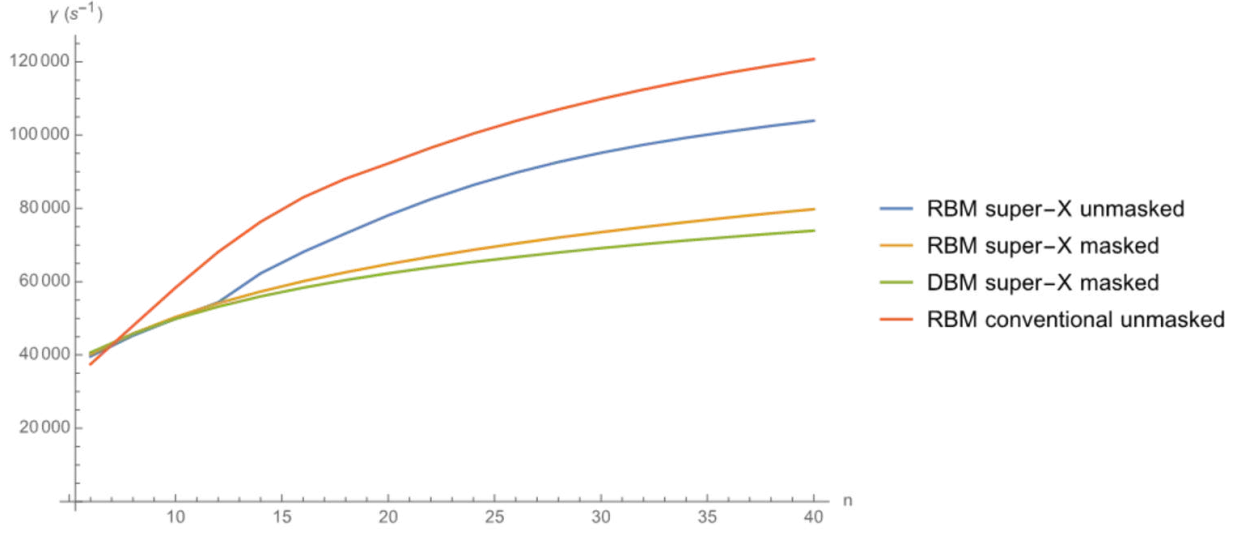
This is the author's peer reviewed, accepted manuscript. However, the online version of record will be different from this version once it has been copyedited and typeset.

PLEASE CITE THIS ARTICLE AS DOI: 10.1063/5.0063766



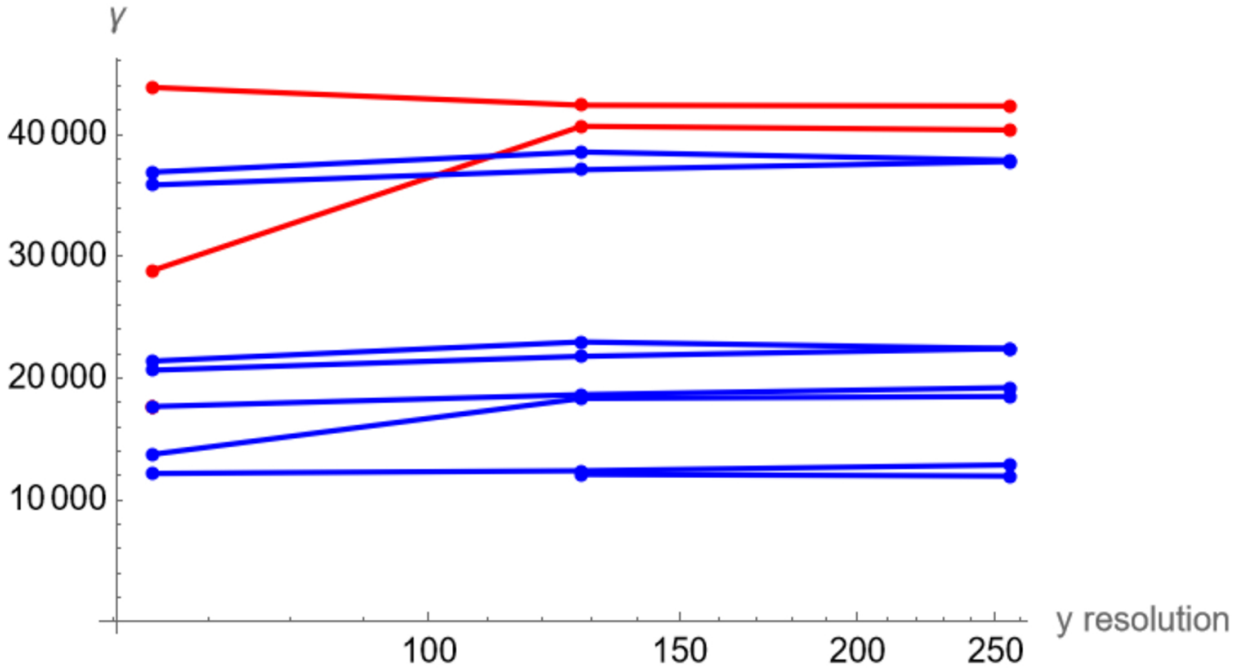
This is the author's peer reviewed, accepted manuscript. However, the online version of record will be different from this version once it has been copyedited and typeset.

PLEASE CITE THIS ARTICLE AS DOI: 10.1063/1.50063766



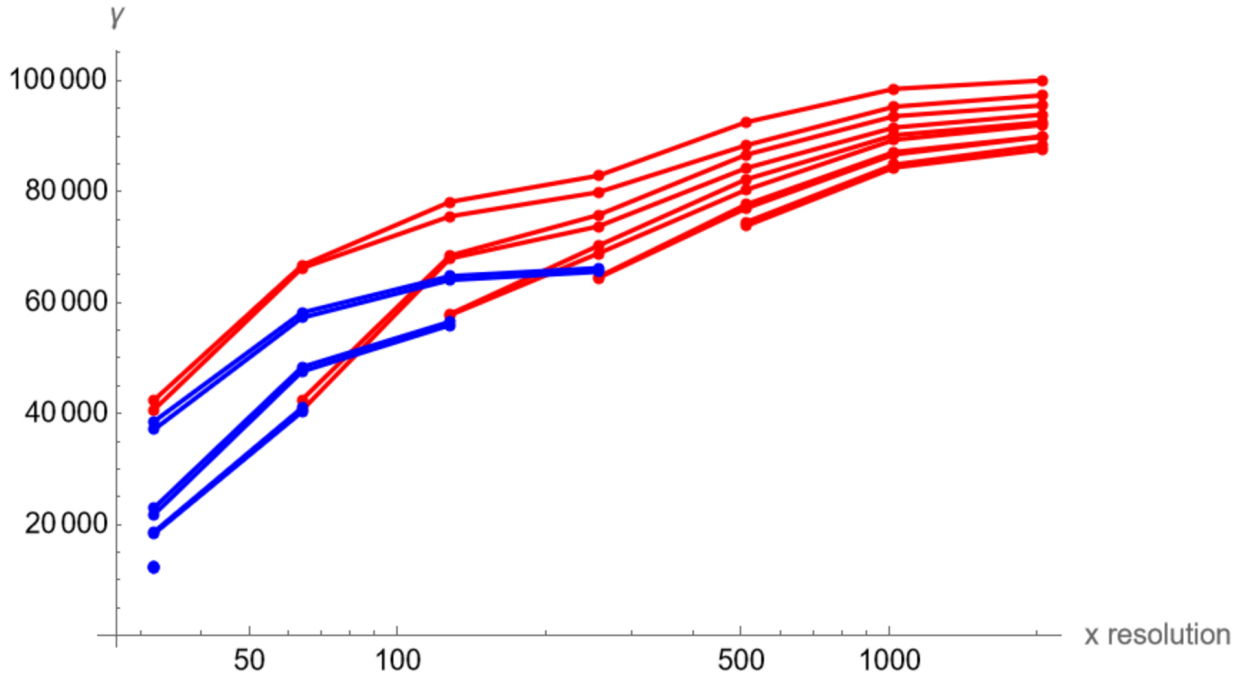
This is the author's peer reviewed, accepted manuscript. However, the online version of record will be different from this version once it has been copyedited and typeset.

PLEASE CITE THIS ARTICLE AS DOI: 10.1063/5.0063766



This is the author's peer reviewed, accepted manuscript. However, the online version of record will be different from this version once it has been copyedited and typeset.

PLEASE CITE THIS ARTICLE AS DOI: 10.1063/5.0063766



This report was prepared as an account of work sponsored by an agency of the United States Government. Neither the United States Government nor any agency thereof, nor any of their employees, makes any warranty, express or implied, or assumes any legal liability or responsibility for the accuracy, completeness, or usefulness of any information, apparatus, product, or process disclosed, or represents that its use would not infringe privately owned rights. Reference herein to any specific commercial product, process, or service by trade name, trademark, manufacturer, or otherwise does not necessarily constitute or imply its endorsement, recommendation, or favoring by the United States Government or any agency thereof. The views and opinions of authors expressed herein do not necessarily state or reflect those of the United States Government or any agency thereof.